Structural insights into pore dynamics of human Pannexin isoforms

Nazia Hussain[1], Ashish Apotikar [1], Pidathala Shabareesh[1,4], Sourajit Mukherjee[1,3], Ananth Prasad Burada[1], Sujit Kumar Sikdar[1], Kutti R. Vinothkumar[2] & Aravind Penmatsa[1]*

Address:

[1] Molecular Biophysics Unit, Indian Institute of Science, Bangalore, 560012

[2] National Centre for Biological Sciences, Tata Institute of Fundamental Research, Bangalore, 560065

Present Addresses.

[3] Department of Chemistry, The University of Chicago, Chicago,

[4] St Jude Children's Hospital, Memphis, Tennessee.

*Corresponding author.

Email. penmatsa@iisc.ac.in; +91 802293 3552

Abstract: Pannexins are structurally related to connexins and innexins but remain as single-membrane large-pore ion channels to release cellular ATP upon activation. There are three isoforms of pannexins, 1, 2, and 3, with diverse cellular roles, including inflammation, differentiation, neuropathic pain, and ATP release. In this study, we report the cryoEM structure of pannexin 3 that displays structural differences with pannexin1 through the presence of a second compartment in the vestibule. We also report the structures of pannexin1 congenital mutant R217H along with a pannexin1 pore mutant W74R/R75D that mimics pannexin2, in the resolution range of 3.8-4.2 Å. The congenital mutant and the pannexin2 mimic induce structural changes that lead to a partially closed pore and alter ATP interaction propensities. The channel conductance of the congenital mutant displays weakened voltage sensitivity. The results signify the vital role of pore-lining residues and their dynamics in dictating pannexins' architecture and physiology.

Keywords. Pannexin1, Pannexin3, ATP-binding, R217H, channel pore, Cryo-EM

Introduction

Pannexins are large-pore vertebrate ion channels identified through sequence similarity with invertebrate gap-junction channels, innexins[1]. Pannexin protomers retain structural and topological similarity to innexins, connexins, and volume-regulated anion channels but remain as single-membrane channels and participate in ion-conductance and ATP release[2]. Three isoforms of pannexins (PANX1, 2 & 3) are identified in mammalian cell types, and each is observed in diverse tissue and physiological niches[3].

Pannexin1(PANX1) is the most widely studied member among pannexins and is ubiquitously present in several tissue types, and is a channel involved in purinergic signaling through ATP release[4]. It is documented to play a role in diverse processes, including inflammation, cell migration, apoptosis, cytokine secretion, and viral replication[5-8]. The C-terminus of PANX1 is susceptible to caspase 3 cleavage that results in channel-opening and ATP release as a "find-me" signal for macrophages to target apoptotic cells[9]. Besides ATP release, PANX1 is also known to display ionic conductance in response to extracellular potassium, a positive voltage, and in some instances, display mechanosensitive properties[10,11]. PANX1 knockout results in diverse phenotypes like hearing loss, weakened epileptic propensity, and reduced ATP/cytokine release[12-14]. A recent identification of a germline mutant of *PANX1* (R217H) that leads to defective channel activity resulting in intellectual disability, ovarian failure, hearing loss, and skeletal defects[15] signifies the importance of PANX1 as an essential player in human physiology.

Recent structural studies on different orthologues of Pannexin1 (PANX1) have shown that the channel is organized as a heptamer[16-18]. The topology is similar to large-pore ion channels with four transmembrane helices (TMs), a prominent extracellular domain (ECD), and a disordered C-terminus that is not visible in most PANX1 structures. The access to the channel vestibule through the cytosol is unhindered except for a constriction point at the ECD that would enforce selective ion/ATP gating depending on the pore radius. This pore, lined by tryptophan residues, is also proposed as the site for carbenoxolone (CBX) interactions that block PANX1[16,19].

A lot less is known about the two other isoforms of PANX1, namely PANX2 and PANX3, which have more tissue-specific expression patterns. PANX2 is primarily expressed in neurons and glial cells and is involved in cellular differentiation[20]. PANX3 is expressed in osteoblasts, chondrocytes, and skin and plays a major role in calcium homeostasis[21]. PANX3 has been observed to regulate osteoblast differentiation through its ER calcium channel function[22]. Along with its predominant role in osteoblast differentiation and wound healing in mice[23], PANX3 also functions as an ATP release channel similar to PANX1, and the released ATP acts as an activator for P2R-PI3K-AKT signaling[22]. PANX3 is closer to

PANX1 in sequence identity and is the shortest among the three isoforms[3]. PANX2 is the most divergent among the three, with sequence identity in the range of 24%, and is characterized by a substantially longer C-terminus[3]. Surprisingly, despite the sequence similarities among PANX isoforms, PANX1, PANX2, and PANX3 harbour diverse residues at the channel pore that likely cause altered behaviour among the three isoforms.

In this study, we present the electron cryomicroscopy (cryo-EM) structures of human Pannexin3 (PANX3) and human Pannexin1 (PANX1) and its mutants to observe altered pore dynamics and also demonstrate the structural effects of these substitutions. The PANX3 structure displays a constriction point below the pore that facilitates the formation of a second vestibular cavity in PANX3. We observe that the congenital mutant R217H ($PANX1_{R217H}$) in TM3, in comparison with $PANX1_{WT,}$ results in allosteric modulation of the PANX1 pore to constrict it further and significantly alter its conductance properties. A pore mimic of PANX2 isoform ($PANX1_{DM}$) in PANX1 results in a highly cationic, narrow pore and subtle shifts to the PANX1 extracellular domain (ECD). We study the alteration of channel properties using electrophysiological measurements and ATP interactions to highlight the effects of substitutions on pore dynamics and channel function among PANX isoforms.

Results

Pannexin3 has altered structural features.

The PANX3 shares 42% sequence identity with PANX1(Extended Data Fig.1). Despite the high sequence conservation with its isoform, PANX3 displays distinct structural features, localization, and functional characteristics compared to $PANX1_{WT}$. To understand the disparity among PANX isoforms, we purified the full-length human PANX3 and determined the structure to an overall resolution of 3.9 Å by cryo-EM in the absence of ATP and calcium ions (Extended Data Fig. 2, Table S1). The PANX3 structure modeled into the density reveals an open conformation of the channel.□□□Clear density at the pore and transmembrane helices allowed accurate modeling of the side chains in these regions (Extended Data Fig. 3a). The intracellular helices (160-185) and the C-terminus (373-392) lack clear densities, likely due to inherent flexibility in this region. The PANX3 protomers retain the heptameric oligomer assembly that can be partitioned into an extracellular domain (ECD), transmembrane domain(TMD), and intracellular domain(ICD), similar to $PANX1_{WT}$ (Fig.1a,b). Unlike other large-pore ion-channels like CALHMs, the PANX isoforms do not display heterogenous oligomeric associations[24]. The PANX3 channel is 8 Å wider than the PANX1 at the cytosolic face with a similar transmembrane height in the ordered regions of the channel. (Fig. 1b, c).

The topology of PANX3 protomers is similar to $PANX1_{WT}$, with differences in the TM1 and the extracellular loops. The topology comprises four transmembrane helices and two

extracellular domains. Two disulfide bonds stabilize the extracellular domains, C66-C261(SS1) and C84-C242(SS2), that form between EL1 and EL2 (Extended Data Fig. 4a, b). The superposition of two protomers (PANX1-PANX3) results in a root mean square deviation (rmsd) of 3.2 Å for the 302 Cα atoms (Fig. 1d). There is also a significant alteration of surface charge within PANX3 compared to $PANX1_{WT}$ near the surface lining the aqueous channel vestibule (Fig. 1e). Although $PANX1_{WT}$ has a positive charge at this position, PANX3 possesses a negatively charged environment that could attract divalent cations like calcium that is suggested to be transported through PANX3. The negatively charged surface in PANX3 may facilitate its role as an ER calcium channel (Fig. 1e).

N-linked glycosylation at the N255 position in the EL2 of PANX1 was implicated in preventing the formation of gap junctions. A substitution at this site (N255A) led to the formation of a mixture of gap junctions and hemichannels[16]. In the PANX3 structure, we observed density for N-acetylglucosamine (NAG) at the predicted glycosylation site (N71) in the first extracellular loop that is much closer to the pore in comparison to PANX1(Fig. 1f).

As we did not observe density for residues 1-24 in N-terminus, it is unclear if the N terminus lines the pore and plays a role in maintaining the rigidity of the transmembrane domain of the heptamer. A comparison with the Alphafold2 model of PANX3 with the experimental model in this study indicates that the N-terminus faces the cytosol. It constricts the channel from the cytoplasmic side, unlike $PANX1_{WT}$, where the N-terminus lines the pore and interacts partially with the adjacent protomer[16]. This disparity among isoforms has been observed in CALHM1 and 2, where the N-terminus of CALHM2 is directed towards the cytosolic side of the channel[25,26]. Towards the C-terminus, we did not observe the density for the last twenty residues (373-392). The C-terminus is comparatively shorter than PANX1 and is unlikely to serve as a plug to block access to the channel, and lacks a caspase cleavage site to facilitate ATP release, as observed in PANX1. Consequently, the short C-terminus in PANX3 is unlikely to play a role in channel opening, and PANX3 may have alternate mechanisms for channel-gating.

PANX3 displays a double-sieve pore organization

The residue lining the constriction point in PANX1, W74, is replaced by isoleucine or valine in different orthologues of PANX3 (Extended Data Fig. 4c). The PANX3's pore is lined by two residues, I74 and R75, with a width of 13.2 Å at the narrowest point (Fig. 2a, b). The primary constriction created by the W74 residue in $PANX1_{WT}$ results in a pore diameter of 12 Å. The presence of I74 in PANX3 instead of W74 widens the pore to a radius of 13.2 Å. The cation-π interaction between W74 and R75 in $PANX1_{WT}$ is altered in PANX3 due to the replacement of W74 with I74. R75 of one protomer interacts with D81 of the other protomer through a salt bridge.

Similarly, S70 and Q76 between two protomers form a hydrogen bond resulting in interprotomeric interactions leading to a stable heptamer. Apart from these interactions, there seem to be minimal intersubunit interactions across the transmembrane region between the protomers. The gap between the TMs 2 and 4 of adjacent protomers just beneath the ECD is occupied by lipid-like density into which we have modeled a phospholipid, 1-palmitoyl-2-oleoylphosphatidylethanolamine (POPE), for each protomer (Extended Data Fig. 3b). We could also observe a gap between subunits that is large enough to allow the passage of ions. The presence of a side-tunnel suggested by Ruan et al. in $PANX1_{WT}$ is more prominent in PANX3, with a 6.9 Å separation between TM2 and CTH1 compared to 6.3 Å in $PANX1_{WT}$, suggesting that the lateral portal hypothesis may also hold true for PANX3 (Extended Data Fig. 4d).

The structural comparison of PANX3 with $PANX1_{WT}$ reveals an additional constriction in PANX3 below the primary channel pore. The residues at the end of TM1, 58-60 comprising residues F58, S59, and S60 forms a prominent second constriction at the neck region in PANX3 compared to $PANX1_{WT}$ (Fig. 2c). The linker between TM1 and TM2 adopts a clear α-helical conformation in PANX3, instead of a loop observed in $PANX1_{WT}$, constricting the vestibule in the region, thus allowing PANX3 to have an additional vestibule beneath the pore (Fig. 2d). The residues F58-S59-S60 line the second constriction point facing the pore in PANX3 and are part of the PANX3 sequence that is highly variable between PANX1, 2 and 3 (Extended Data Fig. 4e). In contrast, I58 residue in $PANX1_{WT}$ participates in hydrophobic interactions between TMs 1 and 2 (Fig. 2c, d). The diameter at this constriction point is 21 Å compared to 30 Å in $PANX1_{WT}$ and demarcates the boundary between the anionic surface of the upper compartment compared to the amphiphilic lower compartment (Fig. 1e). An annulus of seven uncharacterized densities are observed at this constriction point that further contribute to restricting access at this region. Also, the movements of the aromatic group of F58 through its $\chi 1$ torsion angle can further alter the diameter of this constriction point and facilitate selective access to the pore. The lower compartment leading to the cytosol is larger and has a cationic charge that could facilitate ATP interactions. As described earlier, PANX3 has a shorter C-terminus than $PANX1_{WT}$ and may employ the second constriction point as a control point for ATP release. The anionic upper compartment could further contribute to the calcium flux observed through PANX3[22]. We performed a binding analysis of ATP with PANX3 using microscale thermophoresis (MST). The affinity of ATP analog ATP-γS for PANX3 was determined to be 63 µM compared to the 21 µM affinity observed with $PANX1_{WT}$ (Fig. 2e, f). The ATP binding studies suggest a weaker affinity of PANX3 for ATP compared to PANX1.

The different pore-lining residues observed in PANX1 and PANX3 may dictate isoform-specific differences in channel properties as observed in connexin isoforms (Extended Data Fig. 4e)[27]. For instance, current density measurements and I-V curves for PANX3 suggest that it has a similar voltage sensitivity to PANX1 and elicits voltage-sensitive currents at positive potentials (Fig. 2g). We observe weaker CBX sensitivity in PANX3, in comparison to PANX1, likely due to the substitution of W74, which is proposed as the primary binding site for CBX (Extended Data Fig. 5a). The structural differences observed between PANX3 and PANX1 can therefore influence their respective channel activities and, consequently, their physiological properties.

Congenital mutant of Pannexin1 (R217H) influences channel properties

We elucidated the structure of PANX1 R217H substitution to characterize the effects of this congenital mutant and to understand the basis of its defective channel properties. The arginine residue at the 217 position is highly conserved among vertebrate PANX1 orthologues (Extended Data Fig. 6a). The arginine was mutated to a histidine by site-directed mutagenesis. Consistent with the earlier reports[15], we did not observe compromised expression of the $PANX1_{R217H}$ channel compared to $PANX1_{WT}$ (Extended Data Fig. 6b). The protein was purified to homogeneity, and the structure was determined by cryo-EM at a resolution of 3.9 Å, with densities for side chains clearly resolved at the extracellular domain and TM regions (Extended Data Fig. 3c, 7, Table S1). The model was built using the previously reported structure of $PANX1_{WT}$ (PDB ID-6WBF) that was oriented into the $PANX1_{WT}$ cryoEM map that we calculated and refined to a resolution of 3.75 Å. The superposition of $PANX1_{WT}$ and $PANX1_{R217H}$ mutant yielded a Cα rmsd of 1.2 Å for 288 atoms.

We compared the structure of the mutant channel with the $PANX1_{WT}$ to analyze the local and global variations. The structure resembles $PANX1_{WT}$ globally, with changes in ECD, EH1, and the intracellular domain. Extracellular loops and EH1 have an average shift of 1.5-2 Å away from the pore, which along with the slight TM1 movement, is most likely responsible for inducing the change in the W74 position by moving the tryptophan indole ring towards the pore, thereby shortening the pore radius by 4 Å (Fig. 3a, b). The R75 residue interacts with the D81 of the adjacent subunit through a salt bridge, consistent with $PANX1_{WT}$.

As the mutation of R217H is in TM3, we investigated the residues in the vicinity of R217 within a 4 Å radius. The D35 in TM1 interacts with R217 (3.6 Å) in $hPANX1_{WT}$ and forms a H-bond. R217 also interacts with T220 in TM3 and T39 in TM1 through hydrogen bonds (Fig. 3c). Mutating arginine to histidine disrupts the H-bond interaction network within

TMs 1 and 3. The H-bond interaction of T220 in TM3 and T39 in TM1 with R217H is disrupted due to the shorter side chain of histidine compared to arginine. The G44 in TM1 acts as a hinge point; it facilitates the TM1 bending and displacement as a consequence of R217H substitution. The displacement observed in TM1 translates to an outward movement of ECD that allows the W74 to flip towards the pore (Fig 3b).

In comparison to the $PANX1_{WT}$, the W74 shifts by a $\chi 2$ torsion angle of nearly 88.3° towards the pore leading to substantial closure of the pore diameter in PANX1 channels and affecting channel properties (Fig. 3a). We compared the current density of R217H to $PANX1_{WT}$ by electrophysiology experiments. The average current density for $PANX1_{WT}$ was twofold higher than $PANX1_{R217H}$, indicating partial closure of the pore (Extended Data Fig. 5b, c). Although there was a significant decrease in the current density in the R217H mutant, the mutation did not affect the CBX binding, as we could observe the inhibition of $PANX1_{R217H}$ currents by CBX similar to $PANX1_{WT}$ (Fig. 3d, Extended Data Fig. 5a). The G-V curves plotted for $PANX1_{R217H}$ and $PANX1_{WT}$ exhibit a clear distinction in the voltage sensitivity of the mutant channel indicating a decrease in channel conductance (Fig. 3e, Extended Data Fig. 5e).

Binding studies using MST reveal a decreased ATP binding in the mutant compared to $PANX1_{WT}$ (Fig. 3f). Previous studies have shown a decreased ATP release in the $PANX1_{R217H}$ mutant[15], which can be correlated well with our ATP binding data. Altering charged residues in the vestibule affects the electrostatic surface of the PANX1 vestibule significantly. In this context, we explored the effects of substituting other positively charged residues within the vestibule, like R24 (N-terminus) and R128 (TM2), that face the vestibule interior on ATP interaction propensities. The ATP interaction with R24A substitution has a minimal effect on ATP affinity (K_d of 69 µM). However, R128A (TM2) substitution reveals a complete loss of ATP binding, indicating this region's importance for ATP interaction (Extended Data Fig. 6c, d). Substitutions of positive charges in the TM helices around the vestibule, for instance, R217H and R128A seem to influence the surface electrostatics within the vestibule (Fig. 3g). Although the substitution is in the TM3, we detect structural shifts in the ECD indicating allosteric effects of this congenital mutant. We also observe reduced ATP binding, decreased current density, and voltage sensitivity in the mutant channel (Extended Data Fig. 5b, c, e). Such allosteric effects are observed in the case of disease-causing mutants where the mutation site is far from the observed structural changes and affects their functional properties[28]. It was proposed in an earlier study that the $PANX1_{R217H}$ interactions with the C-terminus can cause the altered channel properties in this congenital mutant[29]. Given the allosteric effects of R217H on the pore diameter observed in this study, long-range effects in C-terminus could also drive some of the properties observed with

$PANX1_{R217H}$. However, given the absence of a structured C-terminus in PANX1 structures done so far, the influence of the C-terminus on $PANX1_{R217H}$ structure would remain speculative at this juncture.

A mimic of Pannexin2 pore in PANX1 through W74R/R75D substitution

Besides PANX1 and 3, PANX2 has a unique pore-lining residue that could affect the isoform's channel properties. PANX2, in comparison to PANX1, has rather drastic substitutions to its pore-lining residues in the form of W74R and R75D (Extended Data Fig. 4e). We initiated our study to monitor the effects of PANX2 like substitutions through the alteration of a single residue substitution R75A, in PANX1, equivalent to the R75A substitution of the ZfPANX1, performed earlier[17]. R75 was suggested as a putative ATP binding site through alanine scanning mutagenesis[30]. We, therefore, mutated R75 to alanine and checked its binding affinity with ATP. The MST data suggests a decrease in the binding affinity with $PANX1_{WT}$ (Extended Data Fig. 6e). Although we observe that R75 contributes to ATP binding, R75 does not act as the sole residue for ATP binding. In all likelihood, multiple residues are involved in ATP interactions, and mutating these residues individually reduces ATP binding but does not abolish it entirely. Electrophysiology data shows a two-fold decrease in the current density compared to $PANX1_{WT}$ and is comparable to $PANX1_{R217H}$, suggesting a smaller pore than $PANX1_{WT}$ (Extended Data Fig. 5b, c). G-V curve for R75A is comparable to wild type and reveals that the pore residue R75 does not affect the voltage sensitivity of the channel (Extended Data Fig. 5d), consistent with the findings with zfPANX1[17]. Similar consequences to arginine substitutions in the pore are observed with LRRC8A, where the channel maintains conductance with arginine substitution but loses anion selectivity[31]

In order to study the effects on pore properties in PANX2, we created a PANX1 mimic of PANX2 by substituting W74 and R75 with arginine and aspartate, respectively. The structure of PANX1 with W74R and R75D($PANX1_{DM}$) was determined to a resolution of 4.3 Å (Table S1). The model was built using the previously determined structure of $PANX1_{WT}$ with clear densities for the side chains for residues surrounding the channel pore (Extended Data Fig. 3d, 7). The main interactions at the pore in $PANX1_{WT}$ are W74-R75 cation-pi interaction within the subunit and R75-D81 interaction between two subunits. As these residues were mutated, the interactions are lost in the $PANX1_{DM}$. Interestingly, these interactions are vital to stabilize the heptamer, and the charge reversal mutant R75E does not form stable heptamers[16]. Instead, in $PANX1_{DM}$, D75 of one protomer interacts with R74 of another protomer to stabilize the structure (Fig. 4a, left inset)

Whilst the global structure resembles the $PANX1_{WT}$, the pore diameter was reduced by 4.1 Å to a diameter of 7.9 Å as compared to $PANX1_{WT}$ and is comparable to $PANX1_{R217H}$

(Fig. 4a, right inset; 4b). With the aid of electrophysiology, we explored the effects of these structural changes on channel physiology (Fig. 4c). The data revealed a two-fold reduction in the current density than $PANX1_{WT,}$ which is consistent with the reduction in pore radius (Extended Data Fig. 5b, c). The ATP binding data shows a weakened K_d value of 82 μM, suggesting that ATP interactions are partly affected by PANX2 pore substitutions (Fig. 4d). We observe a decreased inhibition of $PANX1_{DM}$ currents with CBX compared to $PANX1_{WT}$ since the primary binding site for CBX, W74, was substituted to an arginine, (Extended Data Fig. 5a). The normalised G-V curve plotted for the double mutant and R75A shows a similar voltage sensitivity to the wild type (Extended Data Fig. 5d, e); thus, we can infer that the pore substitutions do not influence the voltage-dependent conductance property of the channel.

In conclusion, our structural findings suggest that pore dynamics are inherently linked to residues lining this constriction and can have distant structural effects. It is observed in this study that pore substitutions affect the TM regions, and a substitution that alters the H-bond network with TM regions, as observed in R217H congenital mutant, has dramatic effects in the pore radius leading to some of the physiological consequences observed.

Discussion

In this study, we report the previously unknown structure of PANX3, an isoform of PANX1. PANX3 shows heptameric oligomer assembly consistent with PANX1 but differs in tissue localization[21]. We observe a voltage dependency similar to PANX1 as it responds to positive voltage but has a weaker affinity for ATP. A single phospholipid molecule at the interface of PANX3 protomers likely plays a role in oligomer interactions and could also influence channel function through lipid interactions. Phospholipids have been observed at a similar location in other wide pore channels[16,24]. The pore size of nearly 13.2 Å indicates the conformation of PANX3 to be an open state that can allow the passage of multiple ions, dyes, and possibly ATP.

A unique feature of PANX3 is the second vestibule in the neck region, which has not been previously observed in any other wide pore channel. The region F58-S59-S60 at the neck faces the pore, forming a ring and demarcating PANX3 vestibule into two compartments (Fig 2a & c). Although the pore is quite wide around F58 in PANX3 structure, the flexibility in the side chain can dynamically regulate the size of this constriction point. This could aid in the regulation of PANX3 channel activity, particularly in the context of PANX3 lacking a long C-terminus that is caspase-sensitive, unlike PANX1. The presence of hydrophobic residues at the neck has been observed in ion channels like Bestrophin[32] and

pentameric ligand-gated ion channels (pLGICs)[33]. Hydrophobic constrictions in ion channels can aid in the creation of barriers to ion flow and alter the wettability of the pore[34].

The cryo-EM structure of congenital mutant, $PANX1_{R217H}$, reveals a narrower pore in comparison with $PANX1_{WT}$ as a consequence of the rotation of W74 at its χ1-torsion angle by 88.3° and partially closes the pore. This is facilitated by the outward movement of the extracellular domain away from the pore as a consequence of the R217H substitution in TM3 that locally destabilizes the H-bond network in the TM region. The weakened conductance behavior of this mutant signifies its inability to respond to a voltage similar to $PANX1_{WT}$. The transition in pore diameter as a consequence of the TM substitution indicates the presence of allostery within PANX1 channels. The substitution of charged residues like R217H, R128A, and R24A around the vestibule also alters the surface electrostatics of the internal vestibule of PANX1, which weakens the ability of ATP to interact with the channel.

The PANX2 mimic, W74R/R75D, also exhibits a smaller pore than $PANX1_{WT}$. The PANX2 mimic resembles LRRC8A, where the constriction is lined by a ring of positively charged arginine residues and plays an essential role in anion permeability[31]. In other isoforms of LRRC8, the arginine is replaced by leucine and phenylalanine; a similar hydrophobic substitution can also be seen in PANX3. The closure of the pore is correlated to the weakened current density and a reduced ability to interact with CBX to the pore of PANX1, thereby suggesting that PANX2 channel properties can be very distinct in comparison to PANX1.

An analysis of the pore profiles of all the constructs generated through the program 'Hole' reveal differences in the channel pore of the mutants compared to $PANX1_{WT}$[35]. The main distinction lies in the width of the pore entrance depicting mutants' smaller size than $PANX1_{WT}$. The smallest Van der Waal radii found were 2.3, 2.4, 5.3, and 4.2 Å for $PANX1_{DM}$, $PANX1_{R217H}$, PANX3, and $PANX1_{WT,}$ respectively, at the pore entrance (Fig. 5a-e).

Previous structures of $PANX1_{WT}$ were determined by multiple groups in different conditions. For instance, high K^+ has been used extensively to open the channel[16,18], and C-terminus cleavage has also been shown to increase the current density in whole-cell recordings[16]. However, all the previously determined structures have identical channel organization and similar positions of pore-lining residues[16,18]. In this study, as a consequence of a congenital mutant and a PANX2 mimic, we could successfully observe changes to the pore radius that are consistent with the altered channel behavior of $PANX1_{R217H}$ and also highlight the pore dynamics that could be observed in PANX2.

In conclusion, the study gives insights into the novel aspects of PANX3 organization with the presence of a double-sieve pore organization. We report the dynamics of PANX1 pore in response to direct substitutions and analyse the long-range effects of a congenital mutant, thereby underscoring the interesting structural and functional diversity among PANX isoforms.

Acknowledgments. Research in this manuscript is funded by the MHRD-STARs program individual grant to AP(MoE/STARS1/167). The work in the project was partly funded by the WellcomeTrust/DBT-India Alliance intermediate fellowship to AP(IA/I/15/2/502063). NH is a PhD student funded by the DBT-JRF program (DBT/2017/IISc/877) at IISc. AA is a PhD student funded by the IISc-GATE fellowship. SM was a graduate student at IISc funded by the DST-INSPIRE fellowship. SP was a postdoctoral fellow of the DBT-RA program in biological sciences. APB is an early-career fellow of the DBT-Wellcome Trust India Alliance. We thank Sucharita Bose and the National Electron Cryo-Microscopy facility, BLiSc, Bangalore (DBT/PR12422/MED/31/287/2014), for the screening of grids and data collection. We would like to acknowledge the advanced cryo-EM facility, IISc funded through the DBT-BUILDER program (BT/INF/22/SP22844/2017) and DST-FIST program (SR/FST/LSII-039/2015) for preliminary data collection. Computational support from the high-performance computing facility "Beagle" setup from grants by a partnership between the DBT, India, and the Indian Institute of Science (IISc-DBT partnership program) is acknowledged. The authors would like to acknowledge the DBT-IISc partnership program phase II and the DST-FIST program support for research.

Author Contributions. NH performed the molecular cloning, optimized purification, grid freezing, performed data processing, refinement of PANX structures and data analyses. AA performed and analysed all the electrophysiology experiments under guidance from SKS. SP initiated the cloning of PANX1 gene and optimized heterologous expression. SM performed initial electrophysiology measurements. APB aided in the preliminary experiments with PANX3. VKR performed the data collection, initial data processing and optimization of grid freezing for PANX1. AP designed and planned the project and provided inputs for structure refinement and data analyses. NH and AP wrote the manuscript with inputs from all authors.

Competing Interests. The authors declare no competing interests.

Methods

Plasmids and cloning

Full-length human PANX1 (UniprotID-Q96RD7) and PANX3 (UniprotID-Q96QZ0) were synthesized by Geneart (Invitrogen). The synthesized genes were subcloned into a pEG-Bacmam vector between EcoR1 and Not1 restriction sites with a C-terminal TEV protease site (ENLYFQ) followed by enhanced green fluorescent protein(eGFP) and 8x His-tag[36].

The site-directed mutagenesis was used to generate the mutants by the mega primer-based whole plasmid amplification method. The primers were designed using SnapGene and synthesized by Sigma. The mutations were verified by Sanger sequencing.

Transfections and Florescence-detection Size Exclusion Chromatography

HEK293S GnTI⁻ cells were seeded at a density of $1x10^6$ cells in DMEM medium with 10% FBS. The cells were transfected using lipofectamine 3000 (Invitrogen) according to the manufacturer's protocol. For fluorescence-detection size exclusion chromatography (FSEC), cells were harvested after 36 hours and were solubilized using 200 µl of 25 mM Tris pH 8.0, 100 mM KCl, 1% glycerol, and 10 mM glycodiosgenin (GDN). The solubilized cells were spun down at 66,000g for 1 hour, and the supernatant was loaded onto the superose6 increase 10/300 GL column (GE Healthcare). GFP fluorescence (λ_{Ex}=488 nm, λ_{Em}=509 nm) was monitored to check the elution volume and the homogeneity of the protein.

Protein expression and purification

The protein was expressed using the *Bacmam* system for high-level expression[36]. In brief, *E.coli* DH10bac cells were transformed with a pEG-PANX1/3 vector. Positive colonies were selected based on blue-white screening, and bacmids were isolated and transfected into Sf9 adherent cells using cellfectin (Invitrogen) according to the manufacturer's protocol. Four days post-transfection, cells were visualized for GFP fluorescence under a fluorescence microscope (the presence of green cells implies the presence of the virus). The virus was filtered through a 0.22 µm filter and harvested. Sf9 cells in suspension at a cell count of $2x10^6$ cells per ml were infected for the generation of the P2 virus. Four days after the infection, cells were spun down at 7000 g, and the supernatant was filtered and stored at 4℃, protected from the light.

HEK293S GnTI⁻ cells were grown at 37℃ in Freestyle 293 medium(Invitrogen) supplemented with 1.5% FBS. Cells were infected with the P2 virus at a density of 2.5-3.0 x 10^6 cells per ml. Twelve hours post-transfection, sodium butyrate was added at a final concentration of 5mM, and the temperature was reduced to 32°C. Cells were harvested 60 hours after infection for the enrichment of the membranes, and cells were sonicated for 15 minutes at 35% amplitude; the sonicated cells were centrifuged at 100,000×g for one hour. Membranes were flash-frozen and kept in -80℃ till further use.

The expressed PANX1/3 was extracted from membranes using 10 mM glycodiosgenin(GDN), 25mM Tris pH(8.0), 100 mM KCl. The solubilized membranes were centrifuged at 100,000 × g for one hour. The supernatant was incubated with Nickel-NTA resin (Qiagen) equilibrated with binding buffer for two hours. The protein was eluted in 25 mM Tris pH (8.0), 100 mM KCl, 1% glycerol, 0.3 M imidazole and 100 µM GDN. The eluted protein was treated with TEV protease for C-terminal GFP and 8x-his-tag cleavage.

The GFP cleaved protein was further purified by size exclusion chromatography in 25 mM Tris pH(8.0), 100 mM KCl, 1% glycerol, and 50 µM GDN (SEC buffer) using Superose6 increase 10/300 GL column. The peak fraction was collected and used for grid freezing (Extended Data Fig. 8, Supplementary Fig. S2).

Cryo-EM sample preparation and data collection

The SEC purified PANX1/PANX3 was concentrated to 5 mg/ml using a 100 kDa cut-off concentrator (Millipore). The concentrated protein was centrifuged at 66,000 g for one hour before grid freezing. Quantifoil 300 mesh gold holey carbon grids (R1.2/1.3) were glow discharged in the air for one minute at 25 mA, and the protein (3µl) was loaded on the grid in FEI vitrobot at 100% humidity and 16□ temperature. The grids were blotted for 3.5 s with a wait time was 10 seconds. For the $PANX1_{R217H}$ mutant, samples were applied twice, and grids were blotted sequentially for 2.0 and 3.5 seconds, respectively. The grids were flash-frozen in liquid ethane and were stored in liquid nitrogen till further use.

Data sets were collected on a Titan Krios 300 keV (ThermoFisher) equipped with Falcon 3 or K2 direct electron detectors (Table S1). For $PANX1_{WT}$ and $PANX1_{DM}$, data was collected with the Falcon 3 detector, whereas for $PANX1_{R217H}$ and PANX3, data was collected on the K2 detector in EFTEM mode with a Bioquantum energy filter and 20 eV slit width. The pixel size of 1.07 Å was used for both the detectors and the total electron dose, and the number of frames for different constructs is mentioned in the table (Table S1).

Cryo-EM data processing and model building

PANX1/3 structures were determined using the cryoSPARC version (3.20)[37]. The movies were imported and motion-corrected by patch motion correction, and the contrast transfer function (CTF) was estimated by patch CTF. After manually curating the images, the CTF-estimated micrographs were used for auto-picking by the blob picker. For manual curation, a cut-off of 6Å for CTF estimation and 1.06 for ice thickness was used to remove bad micrographs.

The auto-picked particles were extracted with a box size of 360 pixels and were subjected to 2D classification; two rounds of 2D classifications were done to remove the junk particles. The selected 2D classes were subjected to ab-initio 3D classification. For the ab-initio modeling, the initial and final resolutions were kept at 12 Å and 8 Å, respectively, and the minibatch size of 1000 was used. The high-resolution class was used for non-uniform refinement[38]. The parameters for non-uniform refinement were adjusted to get a higher resolution map. The maximum alignment resolution was changed to the Nyquist limit, the number of extra passes was increased to 2, the initial dynamic mask resolution was changed to 14 Å, and the batch size was kept like that of ab-initio modeling. The model obtained from non-uniform refinement was subjected to local refinement; a separate mask for the local refinement was not generated, and a default mask provided by cryoSPARC was used. For PANX1/3 datasets, heterogeneous refinement did not produce any high-resolution model and thus was not used for the processing. PANX1 structure refinement was performed with C7 symmetry, whereas PANX3 was processed with C1 for the initial refinement; as C7 symmetry could be seen in the ab-initio 3D structure, C7 symmetry was applied during the refinement to improve the resolution. PANX1 mutants were modeled using previously determined structures (PDB-ID-6WBF). The desired residues were mutated, and the changes owing to the mutations were modeled in the cryo-EM density map in Coot[39].

For PANX3, an Alphafold2 monomer was fitted in the map to make a heptamer in Chimera. The model and the map were aligned using autodock in Phenix. The model was built in the density in coot. All the structures were refined using PHENIX real-space refinement[40]. The workflow and the statistics for each construct are summarized in the extended figures and table (Extended Data Fig. 2, 7) (Table S1).

Binding studies with ATP-γs

Binding studies were done using microscale thermophoresis (MST). The protein concentration of 10 nM (calculated for the heptamer) was kept constant for all the studies. The protein was labeled with 10 nM red Tris Pico dye, and Monolith standard treated capillaries were used to detect binding. A non-hydrolyzable ATP analog, ATP-γs, dissolved in SEC buffer, was used as a ligand for the binding studies. The ligand concentration was diluted for the study in 16-serial dilution, with 2 mM as the highest concentration. The final protein concentration was kept at 5 nM. All the experiments were done in triplicates, and data were plotted as a mean of three independent replicates. Errors bars represent s.e.m.

Electrophysiology

HEK293 cells were maintained in DMEM F-12 Ham medium (Sigma) supplemented with 10% fetal bovine serum (GIBCO, heat-inactivated US origin) and 1 % antibiotic-antimycotic solution (Sigma) in a humidified incubator at 37°C with 5% CO_2. The cells were passaged twice a week, and a fraction of the cells were plated onto 35 mm cell culture dishes (Thermofisher). PANX1 and its mutants and PANX3 were transiently transfected into HEK293 cells with an enhanced green fluorescent protein (eGFP) using the transfection agent Lipofectamine 2000 (Invitrogen). The cells expressing GFP were selected for patch clamp electrophysiological recordings after 24-36 hours of transfection.

PANX currents were activated and recorded in whole-cell mode using EPC 800 amplifier (HEKA Elektronik), Digidata 1440A digitizer (Molecular Devices), and pClamp 10 software. To elicit the currents, 400 ms voltage clamp steps were applied from a holding potential of -60 mV to test potentials of -120 to +120 mV in 10 mV increments. The currents were sampled at 20 kHz, and digitally low pass (Bessel) filtered at 3 kHz. The patch electrodes used for electrophysiology experiments were fabricated using borosilicate glass capillaries and had a resistance of 3-5 MΩ when filled with an internal solution. The pipette solution contained in mM) 150 Cesium gluconate, 2 $MgCl_2.6H_2O$, and 10 HEPES (pH adjusted to 7.4 with NaOH). The extracellular solution contained (in mM) 147 NaCl, 2 KCl, 1 $MgCl_2.6H_2O$, 2 $CaCl_2.2H_2O$, 10 HEPES, 13 Glucose (pH adjusted to 7.4 with CsOH)[15]. The effects of carbenoxolone (Sigma) were evaluated at a final bath concentration of 100 µM by adding as a bolus from a stock solution prepared by dissolving it in milli-Q water. The experiments were performed at room temperature (23°C). (Supplementary Fig. S1)

Electrophysiological data were analyzed using Clampfit, Microsoft Excel, and Graphpad Prism. The current-voltage relationships were plotted as normalized steady state current values at the end of the pulse step (at 400 ms) versus the respective voltage step (mV). Current densities (pA/pF) were obtained by dividing the steady state current values(pA) by the cell membrane capacitance (pF). The conductance voltage relationship was plotted to analyze the voltage dependence of channel activation. The conductance (G) was calculated using $I=G(V_t-V_{rev})$, where I is the steady state current value at the test potential V_t, and V_{rev} is the reversal potential. The conductance voltage plot was fitted to a Boltzmann equation: $I=I_{max}/1+\exp((V_t-V_h)/k))$ where I_{max} is the maximum steady state current amplitude, V_h is half maximal voltage for activation(V_{50}), and *k* is the slope factor. The calculated values for all the constructs are mentioned in a table (Fig. 5e). The number of recordings (n) is mentioned in the figure; a two-tailed unpaired t-test is used for calculating the significance, ***$p < 0.001$; n.s., not significant.

Data Availability

The coordinates and maps are deposited in the PDB and EMDB respectively.

References.

1 Panchin, Y. *et al.* A ubiquitous family of putative gap junction molecules. *Curr Biol* **10**, R473-474, doi:10.1016/s0960-9822(00)00576-5 (2000).

2 Ma, W., Hui, H., Pelegrin, P. & Surprenant, A. Pharmacological characterization of pannexin-1 currents expressed in mammalian cells. *J Pharmacol Exp Ther* **328**, 409-418, doi:10.1124/jpet.108.146365 (2009).

3 Penuela, S., Gehi, R. & Laird, D. W. The biochemistry and function of pannexin channels. *Biochim Biophys Acta* **1828**, 15-22, doi:10.1016/j.bbamem.2012.01.017 (2013).

4 Velasquez, S. & Eugenin, E. A. Role of Pannexin-1 hemichannels and purinergic receptors in the pathogenesis of human diseases. *Front Physiol* **5**, 96, doi:10.3389/fphys.2014.00096 (2014).

5 Makarenkova, H. P. & Shestopalov, V. I. The role of pannexin hemichannels in inflammation and regeneration. *Front Physiol* **5**, 63, doi:10.3389/fphys.2014.00063 (2014).

6 Douanne, T. *et al.* Pannexin-1 limits the production of proinflammatory cytokines during necroptosis. *EMBO Rep* **20**, e47840, doi:10.15252/embr.201947840 (2019).

7 Harcha, P. A., Lopez-Lopez, T., Palacios, A. G. & Saez, P. J. Pannexin Channel Regulation of Cell Migration: Focus on Immune Cells. *Front Immunol* **12**, 750480, doi:10.3389/fimmu.2021.750480 (2021).

8 Paoletti, A. *et al.* Editorial: Pannexin-1--the hidden gatekeeper for HIV-1. *J Leukoc Biol* **94**, 390-392, doi:10.1189/jlb.0313148 (2013).

9 Sandilos, J. K. *et al.* Pannexin 1, an ATP release channel, is activated by caspase cleavage of its pore-associated C-terminal autoinhibitory region. *J Biol Chem* **287**, 11303-11311, doi:10.1074/jbc.M111.323378 (2012).

10 Bao, L., Locovei, S. & Dahl, G. Pannexin membrane channels are mechanosensitive conduits for ATP. *FEBS Lett* **572**, 65-68, doi:10.1016/j.febslet.2004.07.009 (2004).

11 Wang, J. *et al.* The membrane protein Pannexin1 forms two open-channel conformations depending on the mode of activation. *Sci Signal* **7**, ra69, doi:10.1126/scisignal.2005431 (2014).

12 Chen, J., Liang, C., Zong, L., Zhu, Y. & Zhao, H. B. Knockout of Pannexin-1 Induces Hearing Loss. *Int J Mol Sci* **19**, doi:10.3390/ijms19051332 (2018).

13 Aquilino, M. S. *et al.* Pannexin-1 Deficiency Decreases Epileptic Activity in Mice. *Int J Mol Sci* **21**, doi:10.3390/ijms21207510 (2020).

14 Pelegrin, P. & Surprenant, A. Pannexin-1 couples to maitotoxin- and nigericin-induced interleukin-1beta release through a dye uptake-independent pathway. *J Biol Chem* **282**, 2386-2394, doi:10.1074/jbc.M610351200 (2007).

15 Shao, Q. *et al.* A Germline Variant in the PANX1 Gene Has Reduced Channel Function and Is Associated with Multisystem Dysfunction. *J Biol Chem* **291**, 12432-12443, doi:10.1074/jbc.M116.717934 (2016).

16 Ruan, Z., Orozco, I. J., Du, J. & Lu, W. Structures of human pannexin 1 reveal ion pathways and mechanism of gating. *Nature* **584**, 646-651, doi:10.1038/s41586-020-2357-y (2020).

17 Michalski, K., Henze, E., Nguyen, P., Lynch, P. & Kawate, T. The weak voltage dependence of pannexin 1 channels can be tuned by N-terminal modifications. *J Gen Physiol* **150**, 1758-1768, doi:10.1085/jgp.201711804 (2018).

18 Deng, Z. *et al.* Cryo-EM structures of the ATP release channel pannexin 1. *Nat Struct Mol Biol* **27**, 373-381, doi:10.1038/s41594-020-0401-0 (2020).

19 Michalski, K. & Kawate, T. Carbenoxolone inhibits Pannexin1 channels through interactions in the first extracellular loop. *J Gen Physiol* **147**, 165-174, doi:10.1085/jgp.201511505 (2016).

20 Swayne, L. A., Sorbara, C. D. & Bennett, S. A. Pannexin 2 is expressed by postnatal hippocampal neural progenitors and modulates neuronal commitment. *J Biol Chem* **285**, 24977-24986, doi:10.1074/jbc.M110.130054 (2010).

21 Ishikawa, M. *et al.* Pannexin 3 and connexin 43 modulate skeletal development through their distinct functions and expression patterns. *J Cell Sci* **129**, 1018-1030, doi:10.1242/jcs.176883 (2016).

22 Ishikawa, M. *et al.* Pannexin 3 functions as an ER Ca(2+) channel, hemichannel, and gap junction to promote osteoblast differentiation. *J Cell Biol* **193**, 1257-1274, doi:10.1083/jcb.201101050 (2011).

23 Zhang, P. *et al.* Pannexin-3 Deficiency Delays Skin Wound Healing in Mice due to Defects in Channel Functionality. *J Invest Dermatol* **139**, 909-918, doi:10.1016/j.jid.2018.08.033 (2019).

24 Drozdzyk, K. *et al.* Cryo-EM structures and functional properties of CALHM channels of the human placenta. *Elife* **9**, doi:10.7554/eLife.55853 (2020).

25 Choi, W., Clemente, N., Sun, W., Du, J. & Lu, W. The structures and gating mechanism of human calcium homeostasis modulator 2. *Nature* **576**, 163-167, doi:10.1038/s41586-019-1781-3 (2019).

26 Ren, Y. *et al.* Cryo-EM structure of the calcium homeostasis modulator 1 channel. *Sci Adv* **6**, eaba8161, doi:10.1126/sciadv.aba8161 (2020).

27 Nielsen, B. S. *et al.* Structural determinants underlying permeant discrimination of the Cx43 hemichannel. *J Biol Chem* **294**, 16789-16803, doi:10.1074/jbc.RA119.007732 (2019).

28 Prabantu, V. M., Naveenkumar, N. & Srinivasan, N. Influence of Disease-Causing Mutations on Protein Structural Networks. *Front Mol Biosci* **7**, 620554, doi:10.3389/fmolb.2020.620554 (2020).

29 Purohit, R. & Bera, A. K. Mutational effects of Pannexin 1 R217H depend on the carboxyl-terminus. *Biochem Biophys Res Commun* **548**, 143-147, doi:10.1016/j.bbrc.2021.02.060 (2021).

30 Qiu, F., Wang, J. & Dahl, G. Alanine substitution scanning of pannexin1 reveals amino acid residues mediating ATP sensitivity. *Purinergic Signal* **8**, 81-90, doi:10.1007/s11302-011-9263-6 (2012).

31 Deneka, D., Sawicka, M., Lam, A. K. M., Paulino, C. & Dutzler, R. Structure of a volume-regulated anion channel of the LRRC8 family. *Nature* **558**, 254-259, doi:10.1038/s41586-018-0134-y (2018).

32 Kane Dickson, V., Pedi, L. & Long, S. B. Structure and insights into the function of a Ca(2+)-activated Cl(-) channel. *Nature* **516**, 213-218, doi:10.1038/nature13913 (2014).

33 Hibbs, R. E. & Gouaux, E. Principles of activation and permeation in an anion-selective Cys-loop receptor. *Nature* **474**, 54-60, doi:10.1038/nature10139 (2011).

34 Aryal, P., Sansom, M. S. & Tucker, S. J. Hydrophobic gating in ion channels. *J Mol Biol* **427**, 121-130, doi:10.1016/j.jmb.2014.07.030 (2015).

35 Smart, O. S., Goodfellow, J. M. & Wallace, B. A. The pore dimensions of gramicidin A. *Biophys J* **65**, 2455-2460, doi:10.1016/S0006-3495(93)81293-1 (1993).

36 Goehring, A. *et al.* Screening and large-scale expression of membrane proteins in mammalian cells for structural studies. *Nat Protoc* **9**, 2574-2585, doi:10.1038/nprot.2014.173 (2014).

37 Punjani, A., Rubinstein, J. L., Fleet, D. J. & Brubaker, M. A. cryoSPARC: algorithms for rapid unsupervised cryo-EM structure determination. *Nat Methods* **14**, 290-296, doi:10.1038/nmeth.4169 (2017).

38 Punjani, A., Zhang, H. & Fleet, D. J. Non-uniform refinement: adaptive regularization improves single-particle cryo-EM reconstruction. *Nat Methods* **17**, 1214-1221, doi:10.1038/s41592-020-00990-8 (2020).

39 Emsley, P. & Cowtan, K. Coot: model-building tools for molecular graphics. *Acta Crystallogr D Biol Crystallogr* **60**, 2126-2132, doi:10.1107/S0907444904019158 (2004).

40 Afonine, P. V. *et al.* Real-space refinement in PHENIX for cryo-EM and crystallography. *Acta Crystallogr D Struct Biol* **74**, 531-544, doi:10.1107/S2059798318006551 (2018).

Figure Legends

Main Figures:

Figure. 1| Structural comparison of PANX1 and PANX3. **a,** The cryo-EM map for PANX1(blue) and PANX3(monomers colored individually) viewed parallel to the membrane plane, the position of lipid-like densities modeled as POPE and glycosylation at N71 is modeled as NAG in PANX3, shown by gray and red, respectively. **b,** The structure of PANX1(PDB ID:6WBF) and PANX3; top and bottom view exhibiting differences in the width in PANX channels. **c,** The side view of PANX structures. **d,** Superposition of PANX1 and PANX3. **e,** Sagittal section of surface electrostatics of PANX1 and PANX3 colored according to potential from -5(red) to +5(blue) ($k_BTe_c^{-1}$) viewed parallel to the membrane plane. **f,** Top view of superposed PANX1 and PANX3 displaying the differences in the position of glycosylation in PANX1(blue) and PANX3(orange).

Figure. 2| PANX3 displays a double sieve organization. **a,** Traverse section in PANX1(blue) and PANX3(orange) displaying the positions of the two constrictions; first constriction is formed by W74 in PANX1 and I74 in pPANX3, I58 forms the second constriction in PANX1 and F58 in PANX3. **b,** A close-up of the first constriction seen from above. **c,** Second constriction formed by F58 in PANX3 and I58 in PANX1 **d,** Superposition of PANX1 and PANX3 displaying the position of residue 58 and 74. **e-f,** Binding affinity with ATP-γs for PANX1 and PANX3 was determined as 21±7 and 63±24 μM, respectively, n=3, error bar

represents SEM. **g,** Current-voltage (IV) plot for PANX3 in presence(gray) and absence of CBX (orange). Each point represents the mean of n=6-8 individual recordings, and the error bar represents SEM.

Figure. 3| PANX1 congenital mutant, $PANX1_{R217H}$ alters channel properties. **a,** A cross-section of superposed $PANX1_{WT}$ (blue) and $PANX1_{R217H}$ (red); the inset shows the residue (W74) involved in the formation of the extracellular entrance of the pore. The dashed line represents the reduced pore distance in $PANX1_{R217H}$. (red); the W74 rotates by 88.3□ by $\chi 2$ torsion angle, reducing the pore radius by 3.8 Å compared to $PANX1_{WT}$. **b,** The density for Trp74 in the mutant. **c,** The structural superposition of $PANX1_{WT}$ and $PANX1_{R217H}$ exhibits a disrupted hydrogen network, owing to the mutation, displayed in the inset; for clarity, only one subunit is shown, and arrows indicate the direction of the movement of the mutant in comparison to $PANX1_{WT}$ **d,** Current-voltage (IV) plot for the mutant with (gray) or without (red) the inhibitor CBX. Each point is a mean of 4 independent recordings, and the error bar represents SEM. **e,** Conductance-voltage(GV-curve) plot for $PANX1_{R217H}$ exhibits a reduction in the voltage sensitivity of the channel, n=4; the error bar represents SEM. **f,** Apparent binding affinity of the $PANX1_{R217H}$ with ATP-γs was determined to be 153±68 µM compared to 21±7 µM of $PANX1_{WT}$, n=3, error bar=SEM. **g,** Surface representation of $PANX1_{WT}$ and $PANX1_{R217H}$ according to the electrostatic surface potential from -5(red) to +5(blue) ($k_B T e_c^{-1}$) viewed parallel to the membrane plane. The residues in the full length PANX1 structure (PDB ID:6WBF) were deleted to mimic $PANX1_{R217H}$ mutant to compare the electrostatic surface potential between the structures.

Figure. 4| A PANX2 pore mimic through W74/R75 substitution **a,** A cross-section of superposed $PANX1_{WT}$ and $PANX1_{DM}$; the left inset displays the interaction between D75 of one protomer(P1) with R74 of another protomer(P2). The reduction of pore diameter is displayed in the right inset. **b,** The density for W74R. **c,** Current-voltage (IV) plot for $PANX1_{DM}$ in the presence (gray) and absence (purple) of the inhibitor, CBX. **d-e,** Binding affinity for the double mutant ($PANX1_{DM}$) with ATP-γs was estimated as 82±66 µM **f,** The structural superposition of the $PANX1_{WT}$ and the mutant displays the changes in the movement leading to the reduced pore size; for clarity, only one subunit is shown.

Figure. 5| Pore profiles generated by hole program. The minimum radius is observed at the first constriction in PANX isoforms. **a,** The minimum radius is 4.9 Å for PANX3 at the constriction formed by I74. **b,** The $PANX1_{WT}$ has a minimum radius of 4.2 Å formed by W74. **c-d,** The constriction points are created by W74 and R74 in $PANX1_{R217H}$ and $PANX1_{DM}$ respectively. The constriction point is 2.35 Å in $PANX1_{DM}$ and 2.4 Å in $PANX1_{R217H}$. **e,** 2D representation of the hole profile. The line represents the minimum radius for $PANX1_{WT}$ at 4.2 Å.

Extended Figures

Extended Data Fig. 1: Multiple sequence alignment of human PANX isoforms. The mutants studied are marked; $PANX1_{DM}$, a PANX2 mimic, represents a double mutant (W74R, R75D). $PANX1_{R217H}$ is a congenital mutant, $PANX1_{R24A}$ is an N-terminus mutant, $PANX1_{R75A}$ is a pore mutant, and $PANX1_{R128A}$ is a substitution at TM2.

Extended Data Fig. 2: CryoEM processing workflow for PANX3; Initial ab-intio was done without symmetry. As seven subunits could be visualized in the ab-initio 3D reconstruction, C7 symmetry was applied for ab-initio and non-uniform refinement for the final reconstruction. A total of 31k particles were used for the final 3D reconstruction.

Extended Data Fig. 3: Representative densities **a,** Representative density for a single subunit for PANX3 at a σ level of 7.0. **b,** The density for the lipid at a σ level of 7.5. **c,** Congenital mutant $PANX1_{R217H}$ at a σ level of 4.5, a single subunit is shown for clarity. **d,** The representative density for a subunit for the PANX2 mimic, $PANX1_{DM}$, contoured at a σ level of 7.5.

Extended Data Fig. 4: Structural features of PANX1 and PANX3 **a,** Topology diagram of PANX1(blue) and PANX3(orange). **b,** The positions of disulfide bonds in PANX3; SS1(66-261), SS2(84-242) **c,** PANX3 displaying a gap between the protomers; the gap is large enough to accommodate ions and can act as a side tunnel; Inset shows the superposition of PANX1 and PANX3 displaying the position of the side tunnel. **d-e,** Multiple sequence alignment showing W74 and I58 is not conserved between PANX1 and PANX3.

Extended Data Fig. 5: Patch clamp studies of PANX1 and PANX3 **a,** Percentage inhibition by a PANX inhibitor, CBX plotted at +100mV for wild-type PANX1, 3 and the mutants, the number of recordings is mentioned in the parenthesis, error bar represents SEM. A two-tailed unpaired t-test is used for calculating the significance, ***$p < 0.001$; n.s., not significant. **b,** Current density is plotted for the $PANX1_{WT}$(n=8) and the mutants, $PANX1_{R75A}$(n=11), $PANX1_{R217H}$(n=6), $PANX_{DM}$(n=11), the error bar represents SEM. **c,** Current density box plot at +100mV for $PANX1_{WT}$ and the mutants; each point represents an individual recording. **d,** Conductance-voltage (GV-curve) plot for $PANX1_{WT}$(n=8), $PANX1_{R75A}$(n=6), and $PANX1_{DM}$ (n=4) suggests that the pore residues are not involved in the voltage sensitivity of the channel. **e,** The normalized G-V values were fitted with the Boltzmann equation, and the voltage at which the half-maximal activation, V50, occurred along with slope factor, *k*, was calculated for all the constructs.

Extended Data Fig. 6: Biochemical analysis of PANX1 mutants **a,** Multiple sequence alignment of $PANX1_{WT}$ displaying arginine conservation at 217 position. **b,** Fluorescence size exclusion chromatography (FSEC) profile for $PANX1_{WT}$ (blue) on superose6 increase column, the heptamer, and the free GFP is marked on the profile. **c,** Microscale thermophoresis profile for $PANX1_{R24A}$ shows the binding of 69 ± 52μM. **d,** A complete loss of binding was observed in TM2 mutant, $PANX1_{R128A}$. **e,** The binding affinity for the putative ATP binding site in PANX1 was determined to be 61± 19 μM, suggesting that R75 is not the sole residue responsible for ATP binding in PANX1.

Extended Data Fig. 7: CryoEM workflow for the $PANX1_{WT}$ and the mutants. **a,** The structure of $PANX1_{WT}$ was determined at a resolution of 3.75 Å with C7 symmetry; a total of 41k particles were used for the 3D reconstruction. **b,** A similar workflow was used for the congenital mutant, $PANX1_{R217H}$; 40K particles were used for the final 3D reconstruction for a final resolution of 3.87 Å. **c,** The PANX2 mimic structure, $PANX1_{DM}$ was determined at a resolution of 4.29 Å with a total of 41K particles. All the processing was done in Cryosparc.

Extended Data Fig. 8: Size exclusion profiles of PANX1 and PANX3 constructs. **a,** Size exclusion chromatography (SEC) profile for the $PANX1_{WT}$ (blue), the fractions used for cryoEM grid preparation are marked. **b,** SEC profile for congenital mutant $PANX1_{R217H}$ is similar to that of $PANX1_{WT}$. **c,** SEC profile for $PANX1_{DM}$, double mutant, the main fraction is taken for the grid freezing. **d,** SEC profile for PANX3, we observed heterogeneity in the protein, and the protein corresponding to PANX3, labeled as cryoEM, was used for grid freezing. **e-g,** SEC profiles for PANX1 mutants used for ATP binding studies, $PANX1_{R24A}$(pink), $PANX1_{R128A}$(gray), and $PANX1_{R75A}$(green). All the proteins were run on a superose6 column.

Supplementary Fig. S1: a, The protocol used for patch clamp is shown; the voltage steps of 10mV were applied from -120 to +120, mock recordings(untransfected HEK cells) were done prior to the $PANX1_{WT}$ and mutant experiments; Representative traces for whole-cell current for HEK cells expressing $PANX1_{WT}$ and the mutants are displayed, 100µM CBX was applied in a bolus mode to study the effect of the inhibitor on PANX channels. **b,** Representative raw trace for patch clamped PANX3 transfected HEK cells with and without the application of CBX.

Supplementary Fig. S2. **a-b,** SDS-PAGE profile for the $PANX1_{WT}$, PANX3 and the PANX1 mutants used in the study.

Table S1. CryoEM data collection and refinement statistics.

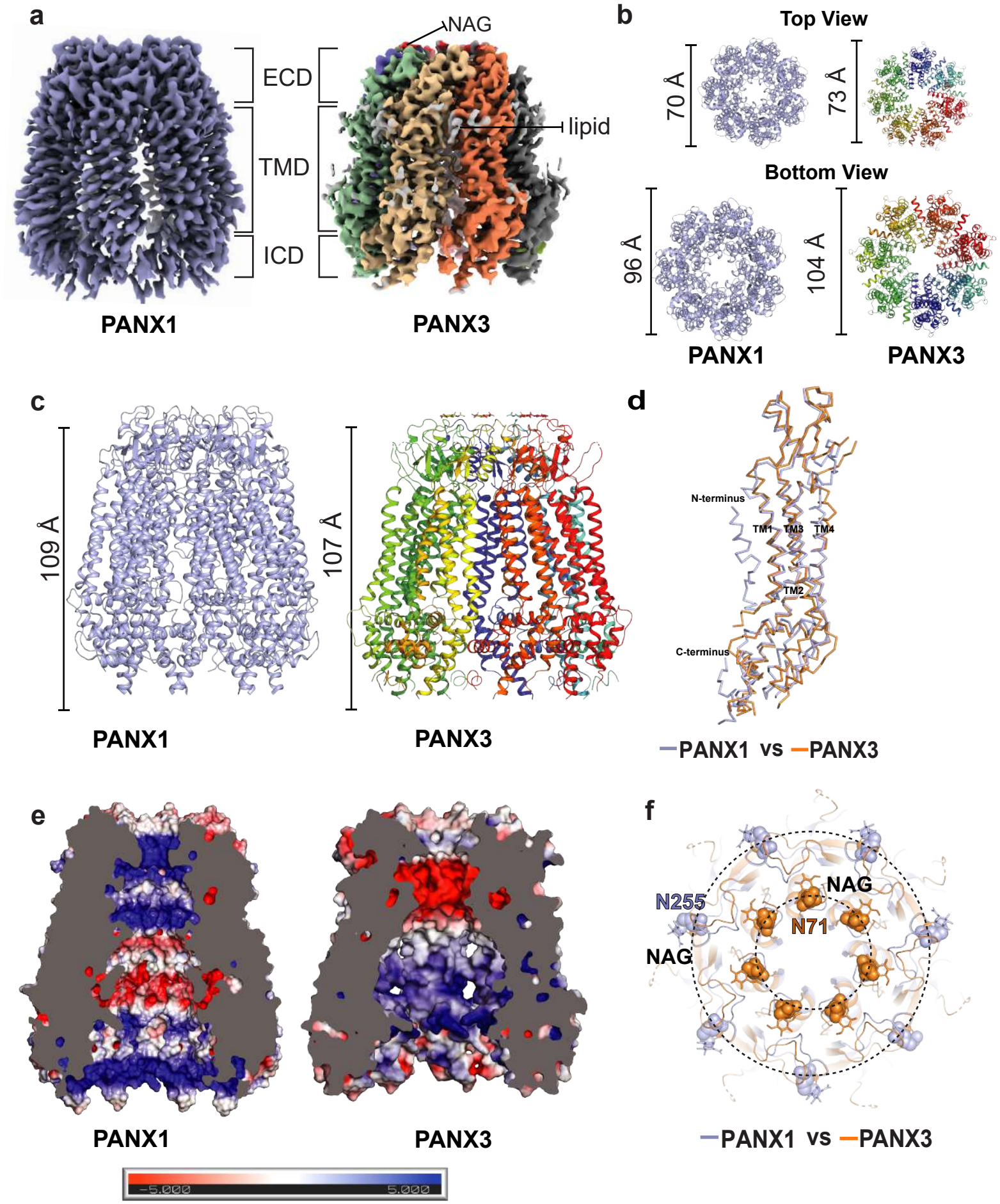

Fig. 1: Structural comparision of PANX1 and PANX3

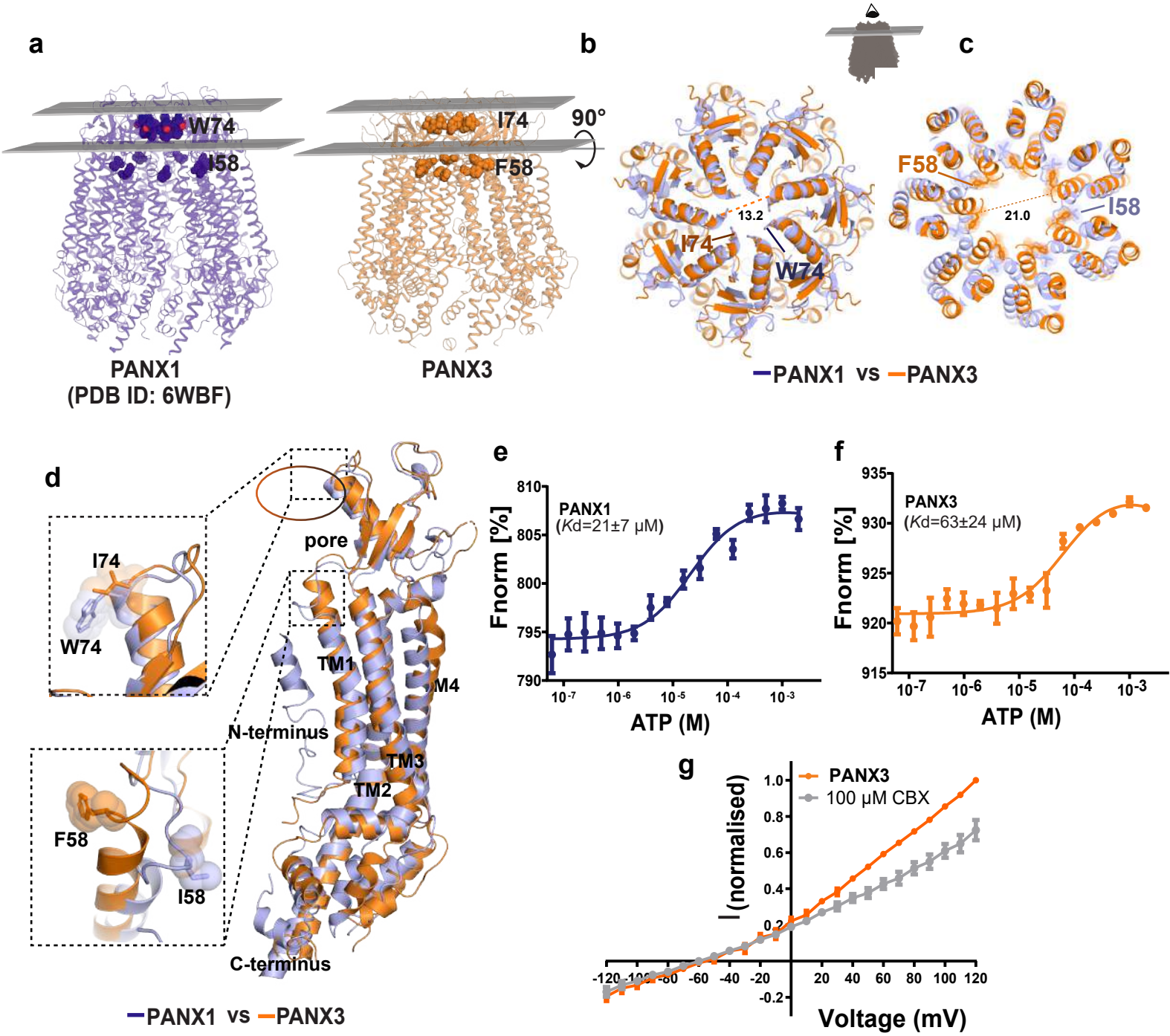

Fig. 2: PANX3 displays double sieve organization.

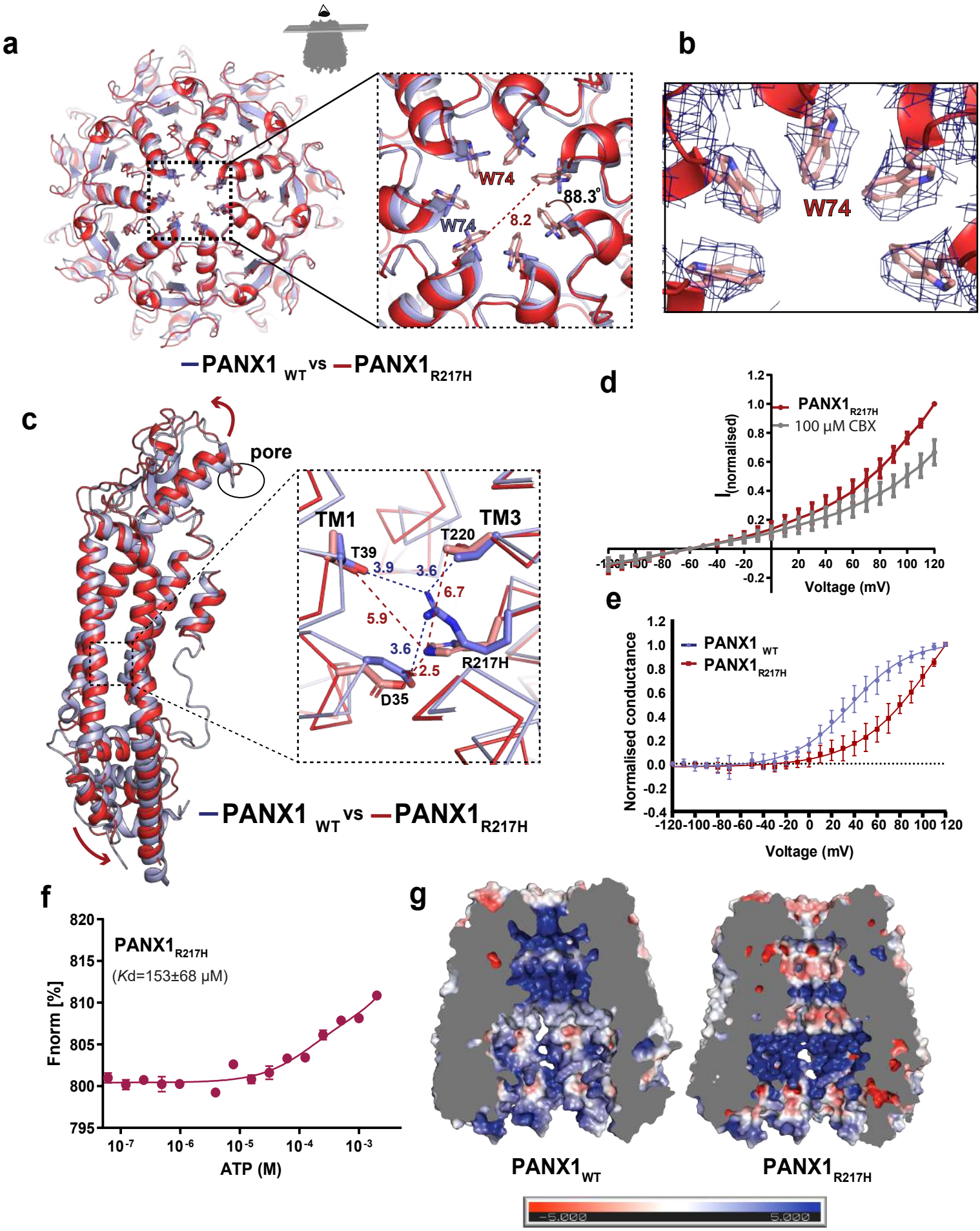

Fig. 3: PANX1 congenital mutant, PANX1$_{R217H}$ influences channel properties.

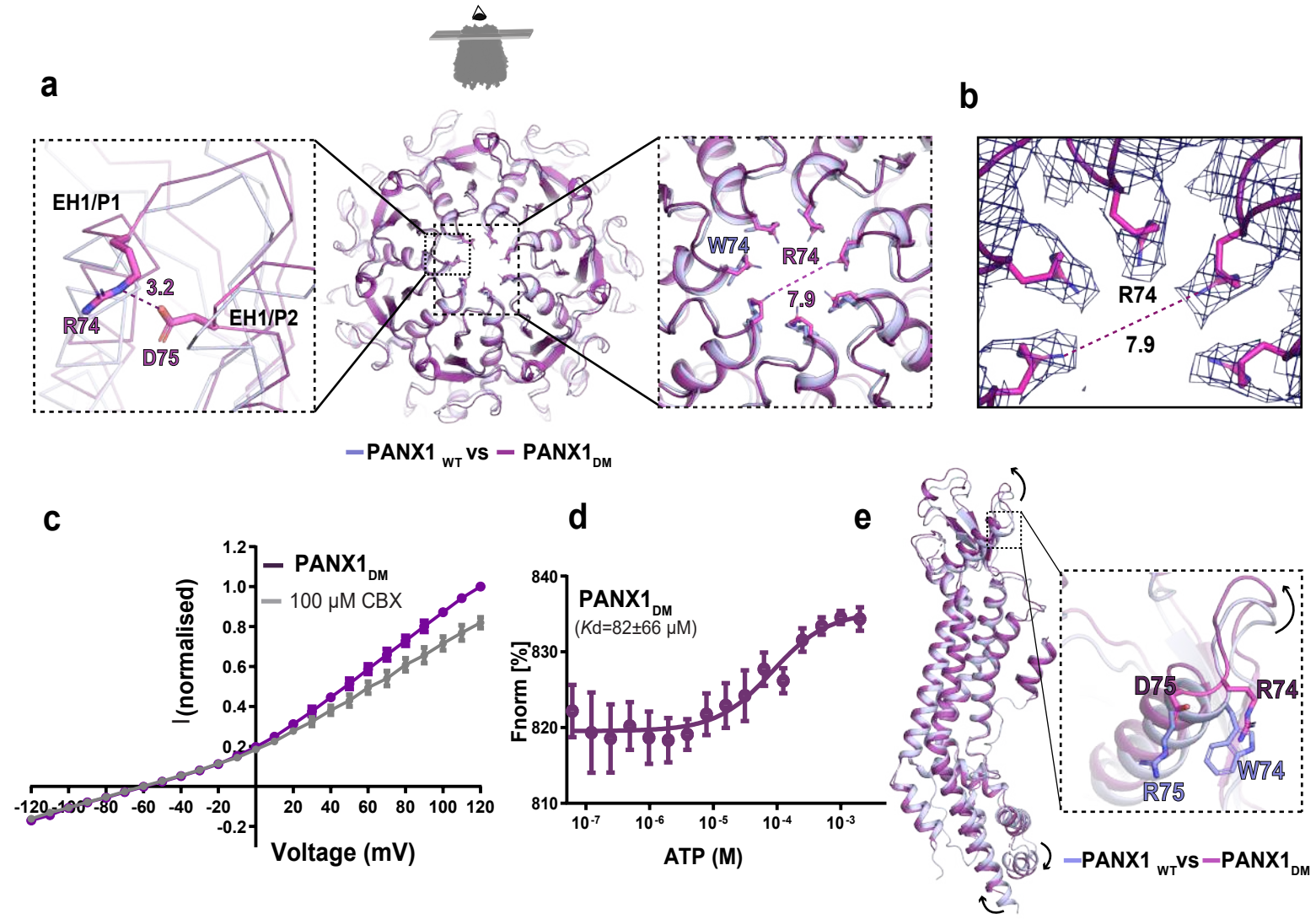

Fig. 4: A PANX2 pore mimic through W74R/R75D substitution.

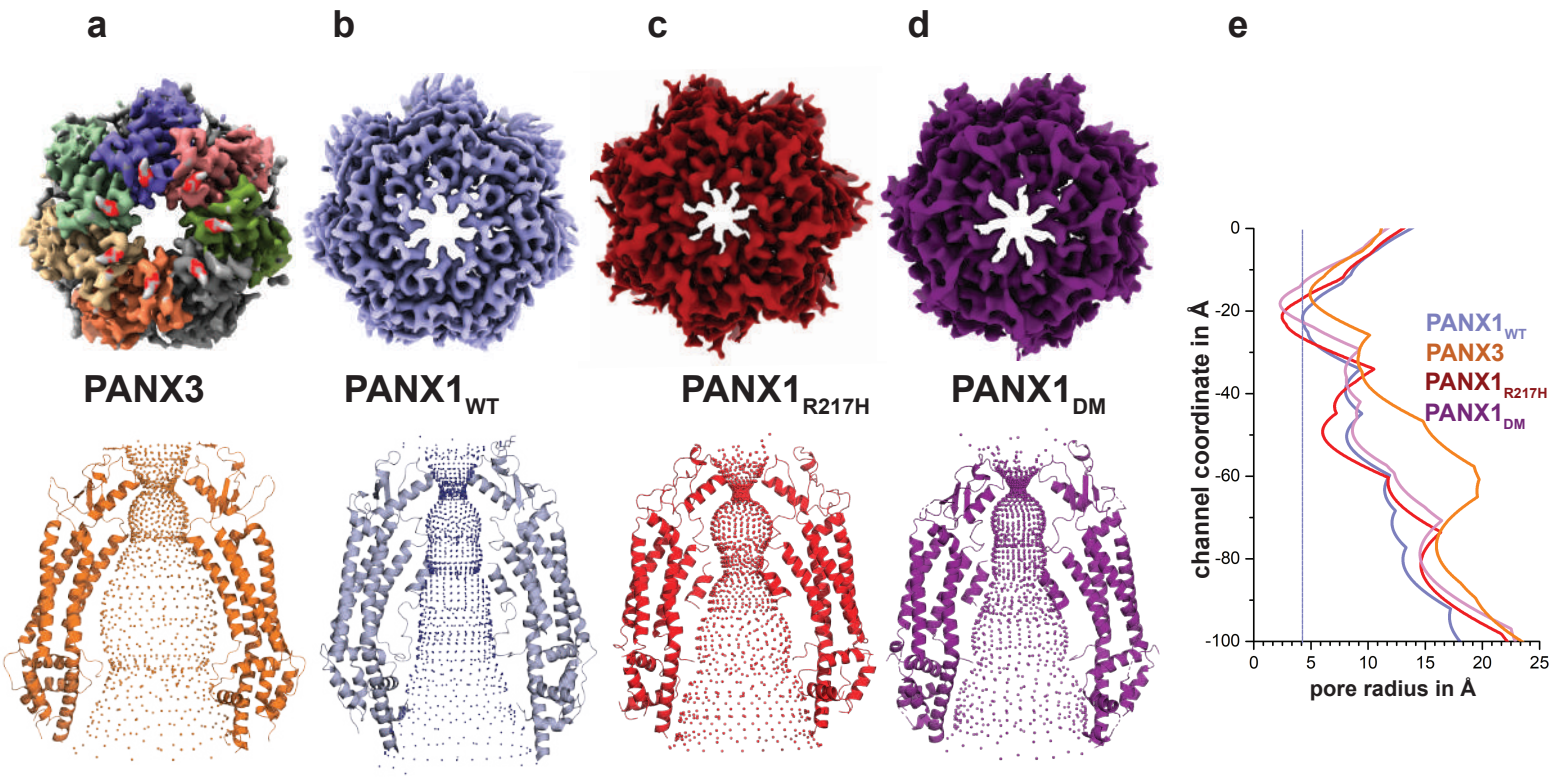

Fig. 5: Pore profiles generated by hole program.